

Experimental Characterization of the High Frequency  
Response of the LHO 4k IFO  
A: Sideband Injection

LIGO-T030163-00-D

William E. Butler and Adrian C. Melissinos  
*Department of Physics & Astronomy,  
University of Rochester, Rochester NY. 14627*

August 7, 2003

# 1 Introduction

In the Fall of 2002 we carried out measurements that contribute to the characterization of the LIGO Hanford 4k Interferometer (LHO 4k IFO).[1] In contrast to previous measurements we examined high frequency signals around the free spectral range (FSR)

$$f_{\text{fsr}} = \frac{c}{2L} = 37.52 \text{ kHz}$$

This work is aimed at establishing the sensitivity and noise level of the IFO to a stochastic background of gravitational radiation at this frequency. Similar measurements were carried out by M. Rakhmanov and R. Savage[2] and a calculation of the sensitivity at the FSR was recently carried out by D. Sigg[3]

A schematic of the LIGO IFO is shown in Fig 1 which can be operated in various configurations including single arm mode and power recycled IFO. The measurements reported in part A were obtained by injecting frequency sidebands upon, (frequency modulation of) the incident light and sweeping around the free spectral range frequency (FSR). This was done in the single arm mode for both the X and Y arms. Sweeping around the 1/2 and 3/2 free spectral range frequencies provides additional information on cavity arm lengths, and the results are particularly sensitive to demodulation phase and to the non-resonant sideband frequency. Pertinent references on cavities, FSR, sidebands and Electro-Optic or Acousto-Optic modulation of light can be found in [4, 5, 6].

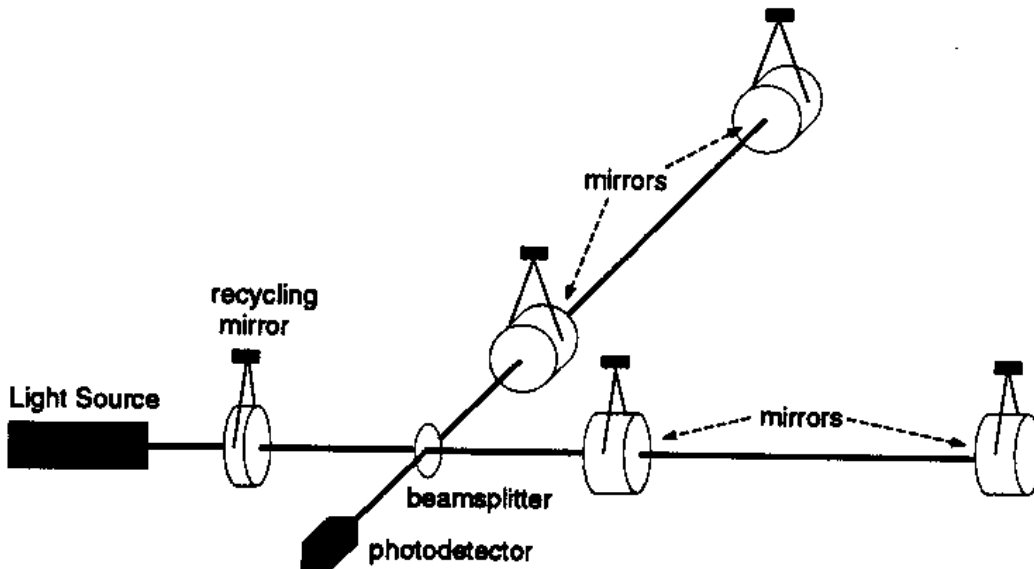


Figure 1: Schematic layout of the Interferometer showing mirror suspensions

The readout of the signal is done via the appropriate RF phase of the demodulated IFO dark port output[7]. For single arm measurements this is the in-phase component, and

for Full-IFO measurements this is the quadrature-phase component. Details about signal readout are given in greater detail in [7, 8]. Appropriate mixing between the I and Q channels is determined as discussed in section 2 and is used for fitting the plots presented in section 3 and 4. For single arm measurements we simply misalign the recycling mirror (RM) and the arm that is not of interest. Then the signal which returns to the dark port (AS) is the reflection off the FP cavity. For full IFO locking all mirrors are aligned and the primary signal of interest (differential arm motion) comes out the AS port. The r.f. output of the diode is taken via cable to a demodulator board, the output of which is processed and digitized for filtering and feedback as well as data analysis. On the demodulator board there are also monitor points where we connected the spectrum analyzer to obtain an analog version of the demodulated output prior to its input into the DAQ (Data Acquisition) system.

The spectrum analyzer that we use (Stanford Research Systems SRS785) can operate in several modes. The primary functions which we use are the FFT and Frequency Response. When we take an FFT we simply look at the output signal in the frequency domain. When we sweep the frequency range of interest then we use the Frequency Response mode. This function takes a series of measurements at different frequencies in which the transfer function from drive to output is measured. In this mode both magnitude and phase response are recorded.

In part B we examine parametric conversion due to the motion of one of the test masses near the FSR frequencies. As a result (audio) sidebands are imposed on the carrier. Obviously there are similarities, but also differences, between sideband injection directly on the carrier and through test mass motion. In the latter case the data are fitted using the program TWIDDLE [9].

In part C we give results on the frequency of the first transverse mode of the arms. We also present data on the excitation of internal modes of oscillation of the test mass and on the up-conversion of the low frequency suspension modes.

## 2 Calculation of Fields

In order to model the response of the IFO to frequency sidebands on the incident light a first order expansion of the fields is sufficient. However one must avoid the assumption that the upper and lower sidebands are equivalent. The signal read out by the diode is the absolute square of the complex field expansion of the light out of the AS port (or reflected off the cavity). This will be of the form<sup>1</sup>  $|E\{J_0(\Gamma_m) + J_1(\Gamma_m)e^{i\omega_m t} - J_1(\Gamma_m)e^{-i\omega_m t}\}\{J_0(\Gamma_s) + J_1(\Gamma_s)e^{i\omega_{rf} t} - J_1(\Gamma_s)e^{-i\omega_{rf} t}\}|^2$  where  $E$  is the unmodulated field. Adopting the notation that a subscript of 0 indicates the carrier field (the corresponding  $e^{i\omega_c t}$  is left off as it conveniently cancels when evaluating the power as it is common to all terms (r.f. and modulation frequencies are put on relative to the carrier frequency), a subscript of ‘m’ indicates the applied modulation frequency, a subscript of ‘s’ indicates the non-resonant r.f. sidebands on the light

---

<sup>1</sup>For pure phase modulation we adopt the convention of the sidebands being real, the upper one positive and the lower one negative.

necessary for locking the cavity by an optical heterodyning technique[8]. A subscript of 'a' indicates the sideband at the sum of the r.f. and modulation frequencies, and 'b' indicates the sideband at the difference of the r.f. and modulation frequencies. It is also necessary to distinguish between the upper and lower sidebands as they obtain different phases upon reflection from the cavity (indicated by a '+' for the upper sideband and a '-' for the lower). Thus the signal is proportional to:

$$AS_{\text{rf}} = \left| \begin{array}{l} E_0 + E_{m+}e^{i\omega_m t} - E_{m-}e^{-i\omega_m t} + E_{s+}e^{i\omega_s t} - E_{s-}e^{-i\omega_s t} \\ + E_{a+}e^{i(\omega_s+\omega_m)t} + E_{a-}e^{-i(\omega_s+\omega_m)t} - E_{b+}e^{i(\omega_s-\omega_m)t} - E_{b-}e^{-i(\omega_s-\omega_m)t} \end{array} \right|^2 \quad (1)$$

Where all E-fields specified are the fields reflected off the cavity. Reflection off a simple Fabry Perot cavity is given by

$$\frac{E_r}{E_0} = \frac{r_1 - r_2(r_1^2 + t_1^2)e^{-i\phi}}{1 - r_1 r_2 e^{-i\phi}} \quad (2)$$

This is derived in [10] which also includes expressions for the other fields. The parameter  $\phi$  is nominally  $2L\omega/c$  where  $L$  = length of the cavity. This was simulated in software by  $\phi = 2\pi x/f_{\text{fsr}}$  where  $f_{\text{fsr}} = c/2L$ .

The output of the photo-diode is sent through a bandpass filter to limit the signal to the range of interest around the r.f. sideband frequency. Thus after demodulation the signal of interest is once again at the applied modulation frequency. So I take equation 1 and expand it while keeping only the terms at  $\pm(\omega_s \pm \omega_m)$  then separate it out so that it can be written in terms of  $\cos(\omega_s t)$  and  $\sin(\omega_s t)$ . The result is (where \* indicates the complex conjugate field):

$$AS_{\text{rf}} = \cos(\omega_s t) \left[ \begin{array}{l} e^{i\omega_m t} \left( \begin{array}{l} E_0^* E_{a+} + E_0 E_{a-}^* - E_{m+} E_{s-}^* - E_{m-}^* E_{s+} \\ - E_0^* E_{b-} - E_0 E_{b+}^* + E_{m+} E_{s+}^* + E_{m-}^* E_{s-} \end{array} \right) \\ + e^{-i\omega_m t} \left( \begin{array}{l} E_0^* E_{a-} + E_0 E_{a+}^* - E_{m-} E_{s+}^* - E_{m+}^* E_{s-} \\ - E_0^* E_{b+} - E_0 E_{b-}^* + E_{m-} E_{s-}^* + E_{m+}^* E_{s+} \end{array} \right) \end{array} \right] \\ + i \sin(\omega_s t) \left[ \begin{array}{l} e^{i\omega_m t} \left( \begin{array}{l} E_0^* E_{a+} + E_0 E_{a-}^* - E_{m+} E_{s-}^* - E_{m-}^* E_{s+} \\ + E_0^* E_{b-} + E_0 E_{b+}^* - E_{m+} E_{s+}^* - E_{m-}^* E_{s-} \end{array} \right) \\ + e^{-i\omega_m t} \left( \begin{array}{l} -E_0^* E_{a-} - E_0 E_{a+}^* + E_{m-} E_{s+}^* + E_{m+}^* E_{s-} \\ - E_0^* E_{b+} - E_0 E_{b-}^* + E_{m-} E_{s-}^* + E_{m+}^* E_{s+} \end{array} \right) \end{array} \right] \quad (3)$$

We may write Eq.(3) compactly as

$$AS_{\text{rf}} = \cos(\omega_s t)[e^{i\omega_m t}(\alpha) + e^{-i\omega_m t}(\beta)] + i \sin(\omega_s t)[e^{i\omega_m t}(\gamma) + e^{-i\omega_m t}(\delta)] \quad (4)$$

where we substitute  $\alpha$ ,  $\beta$ ,  $\gamma$  and  $\delta$  for the corresponding sets of field terms. Upon closer inspection of Eq.(3) it is apparent that  $\beta = \alpha^*$  and  $\delta = -\gamma^*$ , so that Eq.(4) can be further simplified to

$$\begin{aligned} AS_{\text{rf}} &= \cos(\omega_s t)[\alpha e^{i\omega_m t} + \alpha^* e^{-i\omega_m t}] + \sin(\omega_s t)[i\gamma e^{i\omega_m t} - i\gamma^* e^{-i\omega_m t}] \\ &= 2 \cos(\omega_s t)\mathcal{Re}\{\alpha e^{i\omega_m t}\} + 2 \sin(\omega_s t)\mathcal{Re}\{i\gamma e^{i\omega_m t}\} \end{aligned} \quad (5)$$

In-line demodulation selects the term oscillating as  $\sin(\omega_s t)$  while quadrature demodulation selects the term oscillating as  $\cos(\omega_s t)$ . Thus the demodulated signals are

$$\begin{aligned} \text{AS\_I} &= \Re\{i\gamma e^{i\omega_m t}\} \\ \text{AS\_Q} &= \Re\{\alpha e^{i\omega_m t}\} \end{aligned} \quad (6)$$

Spectral analysis of these signals at the frequency  $\omega_m$  yields the magnitude and phase of the complex amplitudes  $i\gamma$  and  $\alpha$  respectively. These amplitudes are defined in Eq.(3) and are frequency dependent because the fields in Eq.(3) are reflected fields.

So far we have assumed that the phase of the demodulating r.f. coincided exactly with the phase of the r.f. component of the detected signal. This is not always the case and a possible phase difference  $\phi$  may exist. Thus

$$\begin{aligned} \text{AS\_I}(\phi) &= \frac{1}{T} \int_0^T \text{AS}_{\text{rf}} \sin(\omega_s t + \phi) \\ \text{AS\_Q}(\phi) &= \frac{1}{T} \int_0^T \text{AS}_{\text{rf}} \cos(\omega_s t + \phi) \end{aligned} \quad (7)$$

where  $T = 2\pi/\omega_s$  and we assume integration over multiples of the r.f. period. Expanding the sine and cosine we immediately find that

$$\begin{aligned} \text{AS\_I}(\phi) &= \Re\{(i\gamma \cos \phi + \alpha \sin \phi) e^{i\omega_m t}\} \\ \text{AS\_Q}(\phi) &= \Re\{(\alpha \cos \phi - i\gamma \sin \phi) e^{i\omega_m t}\} \end{aligned} \quad (8)$$

We have fitted the data to the complex amplitude indicated in Eq.(8) where  $\alpha$  and  $i\gamma$  are given by Eq.(3). As a simple example we can consider the case when the injected sideband frequency is far from  $f_{\text{fsr}}$  (resonance). Then the reflected fields are approximately the same as the incident fields (except for the carrier which is reversed). Thus we can take the fields as real and write

$$\begin{aligned} E_0 &\simeq -1 & E_{s+} &\simeq E_{s-} \simeq \Gamma_s & E_{m+} &\simeq E_{m-} \simeq \Gamma_m \\ E_{a+} &\simeq E_{a-} \simeq & E_{b+} &\simeq E_{b-} & & \Gamma_m \Gamma_s \end{aligned}$$

It then follows that

$$\alpha \simeq 0 \quad \gamma \simeq -8\Gamma_m \Gamma_s \quad \text{far off resonance} \quad (9)$$

When the injected sideband equals  $f_{\text{fsr}}$  then also  $E_{m+}$  and  $E_{m-}$  change sign, and it follows that

$$\alpha \simeq 0 \quad \gamma \simeq 0 \quad \text{on resonance} \quad (10)$$

### 3 Response to sideband injection at $f_{\text{fsr}}$ and $2f_{\text{fsr}}$

The primary method of injecting the sidebands is through the use of the Mode Cleaner feedback circuit which at this frequency feeds back almost directly to the VCO controlling the laser frequency. This has the disadvantage of suffering from a non-linear transfer function from drive to output. However it has the advantage of providing an injection point that does not disturb the control system. A different injection point was considered which in principle had a flat drive with respect to frequency, however the DC shift caused by connecting the readout instruments generally resulted in causing the IFO to lose lock. The modulation frequency was swept (“swept sine” mode) between two limits and the magnitude and phase of the transfer function was recorded by the spectrum analyzer.

Data for the X-arm are shown in Figs (2,3) and for the Y-arm in Figs (5,6,7). The fitting was done in MATLAB to the form<sup>2</sup>

$$\text{fit} = x1 \times (\text{fpi}(f, x2) + x3) \quad (11)$$

where fpi is the calculated signal for pure I-phase [Eqs.(3,6)] and

- $x1$  = overall normalization to account for different gains
- $x2$  = the demodulation phase  $\phi$  in degrees
- $x3$  = a background (noise) level

In addition to optimizing  $x1$  through  $x3$  the fit sought the best value of arm length and of the initial phase. The results returned by the fit are indicated in the figures.

In Figs 2 and 3 the magnitude was fit and the initial phase angle was determined by comparing the data & initial fit at the first data point. Thus the final fit is the initial fit multiplied by a complex number of magnitude 1 and phase of the initial phase (in degrees). It was found necessary to include a  $1/f$  dependence to account for the response of the servo loop. This was achieved in practice by multiplying the data points by  $f$ .

In the X-arm measurements the demod phase  $\phi$  is sufficiently small so that there is essentially no signal in the Q-phase channel, as suggested by introducing the result of Eq.(9) into Eq.(6). The I-phase signal shows a sharp dip at the  $f_{\text{fsr}}$  as suggested by Eq.(10), and provides a very accurate measure of the arm length.

Fig. 2 is a combination of several runs and contains a total of 2,000 data points. The data can not be distinguished from the fit except in the wings of the plot. To estimate the error on the fitted parameters we form the  $\chi^2$  of the fit by assigning equal errors to each data point such that  $\chi^2/\text{DF} \simeq 1$ . A plot of  $\chi^2$  as a function of X-arm length is shown in Fig. 4, and we take the one standard deviation error to be given by the values that increase  $\chi^2$  by one unit. We find for the two arms

$$L_x = 3995.05948 \pm 0.00006 \text{ m}$$

$$L_y = 3995.01332 \pm 0.00041 \text{ m}$$

---

<sup>2</sup>It is necessary to include  $x3$  in the high resolution fig (Fig. 2) to account for very slight effects near resonance.

The above values are, of course, directly dependent on the accuracy of the frequency of the injected sidebands. This frequency is read off the spectrum analyzer and at this point can not be trusted to better than  $1/10^6$ .

For the Y-arm measurements the demodulation phase is sufficiently different from zero so that both the I-phase and Q-phase show a signal. The resulting phase error as extracted from the data is  $\phi \simeq 6$  degrees. During the measurements of the Y-arm, instead of the phase of the transfer function, the absolute phase of the response was recorded. This manifests itself in that the measured phase has a large monotonic increase corresponding to the phase of the drive signal.

## 4 Response to sideband injection at $1/2 f_{\text{fsr}}$ and $3/2 f_{\text{fsr}}$

The injected sidebands would resonate at half-integer values of  $f_{\text{fsr}}$  if the r.f. sidebands were exactly anti-resonant. This is not the case and therefore the sidebands resonate at two nearby frequencies as can be understood intuitively.

If we designate by  $\lambda_s, f_s$  the wavelength and frequency of the r.f. sidebands, exact anti-resonance would imply

$$\lambda_s \left( N + \frac{1}{2} \right) = 2L$$

or

$$f_s = \left( N + \frac{1}{2} \right) f_{\text{fsr}}$$

with  $N$  an integer, and as usual  $f_{\text{fsr}} = c/2L$ . In practice the r.f. frequency is chosen to deviate from the above condition by a frequency decrement<sup>3</sup>  $\Delta$

$$f_s = \left( N + \frac{1}{2} \right) f_{\text{fsr}} - \Delta \tag{12}$$

Resonance will occur when the injected sideband frequency,  $f_m$ , satisfies

$$f_s \pm f_m = \left( N + \frac{1}{2} \right) f_{\text{fsr}} \pm f_m - \Delta = \begin{cases} (N+1)f_{\text{fsr}} \\ Nf_{\text{fsr}} \end{cases}$$

or equivalently

$$\begin{aligned} f_m^+ - \Delta &= \frac{1}{2}f_{\text{fsr}}, \frac{3}{2}f_{\text{fsr}}, \text{ etc...} \\ f_m^- + \Delta &= \frac{1}{2}f_{\text{fsr}}, \frac{3}{2}f_{\text{fsr}}, \text{ etc...} \end{aligned} \tag{13}$$

It follows that the two resonant peaks are separated by

$$f_m^+ - f_m^- = 2\Delta$$

---

<sup>3</sup>To avoid feedback problems caused by allowing the second order sidebands to be resonant.

which is measured experimentally to be of the order  $\Delta = 456$  Hz. From Eq.(12) which defines  $\Delta$  we see that it depends on both  $f_s$  and  $f_{\text{fsr}}$ . Indeed the error on  $\Delta$  is given by

$$\delta\Delta \simeq f_s \left[ \frac{\delta f_{\text{fsr}}}{f_{\text{fsr}}} - \frac{\delta f_s}{f_s} \right] \quad (14)$$

The data are shown in Figs 8,9 for  $f_m \simeq 1/2f_{\text{fsr}}$  and in Figs 10,11 for  $f_m \simeq 3/2f_{\text{fsr}}$ . They were obtained with only the X-arm locked. Note that there is signal in both the I-phase and in the Q-phase. Furthermore the “shape” of the response is extremely sensitive to the demodulation phase.

The fits to the data are done in the same way as discussed in section 3 using the expression for the signals derived in section 2 Eqs.(3 - 8). However now the fit must also optimize the r.f. frequency because the reflected fields  $E_a$  and  $E_b$  in Eqs.(1 - 3) become strongly frequency dependent. As before the fits are excellent and return an average demodulation phase  $\phi \simeq -10$  degrees and an r.f. frequency

$$f_s = 24,481,843 \pm 1 \text{ Hz} \quad (\text{derived})$$

The derived value of  $f_s$  differs significantly from the directly measured<sup>4</sup> value of  $f_s$

$$f_s = 24,481,698 \text{ Hz} \quad (\text{measured})$$

We thus must assign the observed difference to an error in the  $f_{\text{fsr}}$  reading obtained from the spectrum analyzer. According to Eq.(14), this error amounts to  $\delta f_{\text{fsr}}/f_{\text{fsr}} \simeq 6 \times 10^{-6}$ ; large, but not out of the realm of possibilities for an uncalibrated instrument.

## 5 Conclusions

The presence of dips (cancellation) for sidebands injected at  $f_{\text{fsr}}$  has been known for a long time [11, 9, 12, 13], however we believe this to be the first systematic experimental study of these effects [14]. The measurements confirm the theory to a great accuracy and this reflects the advanced status of alignment and control of the IFO.

Perhaps the most interesting conclusion is that the laser phase noise has a minimum at  $f_{\text{fsr}}$ . This is to be expected from our analysis, since the sidebands imposed by phase noise are symmetric and amplitude noise is greatly attenuated at  $f_{\text{fsr}}$ .

In Fig 12 we show the noise floor around  $f_{\text{fsr}}$  and a 6 db drop is clearly observed. Such reduction in noise may facilitate the detection of a stochastic G.W. background signal at  $f_{\text{fsr}}$ , where the response of the IFO is enhanced [12].

---

<sup>4</sup>Which was later checked against a Rubidium standard (Stanford FS725) and found to have an error  $\simeq 1/10^6$ .



## 6 Acknowledgments

We are indebted to the entire Hanford LIGO team for the excellent operation of the IFO and for their support; to Fred Raab for contributing to the early phases of this research and for his hospitality. We acknowledge useful discussions with F. Bondu, W. Kells, M. Landry, M. Rakhmanov, R. Savage and D. Sigg on many aspects of this work.

## References

- [1] B. Barish and R. Weiss. LIGO and the detection of gravitational waves. *Physics Today*, 52:44, 1999. <http://www.ligo.caltech.edu/>.
- [2] Rick Savage. LHO detector e-log entries. Reference arm length measurement on 4th, October 2002.
- [3] Daniel Sigg. Strain calibration in LIGO. Technical report, LHO Hanford, March 1993. LIGO Internal #: T970101.
- [4] Baha E.A. Saleh and M.C. Teich. *Fundamentals of Photonics*. Wiley-Interscience, John Wiley & Sons, INC., 1991. ISBN = 0-471-83965-5.
- [5] Anthony E. Siegman. *LASERS*. University Science Books, 55D Gate Five Road Sausalito, California 94965, 1986.
- [6] Frank L. Pedrotti and Leno S. Pedrotti. *Introduction to Optics*. Prentice Hall, Upper Saddle River, New Jersey 07458, 1993. ISBN = 0-13-501545-6.
- [7] Martin W. Regehr. *Signal Extraction and Control for an Interferometric Gravitational Wave Detector*. PhD thesis, California Institute of Technology, 1995.
- [8] ISC team. Length sensing & control subsystem final design. Technical report, Caltech, July 1998. LIGO Internal #: T980068-00-D.
- [9] Martin W. Regehr, James E. Mason, and Hiro Yamamoto. Twiddle (ver. 3.0) a program for analyzing interferometer frequency response (mathematica 3.0). Technical report, Caltech, February 1999. LIGO Internal #: T990022.
- [10] William E. Butler. Field calculations for a power recycled michelson interferometer with fabry-perot arms, a first principles approach. Technical report, University of Rochester, Dept. of Physics & Astronomy, May 2001. LIGO Internal #: T030162.
- [11] Brian J. Meers. *Some Aspects of the Development of an Optically Sensed Gravitational-Wave Detector*. PhD thesis, Glasgow University, 1983.
- [12] Daniel Sigg and ISC Group. Frequency response of the LIGO interferometer. Technical report, LHO Hanford, February 1997. LIGO Internal #: T970084.
- [13] M. Rakhmanov, R.L. Savage Jr., D.H. Reitze, and D.B. Tanner. Dynamic resonance of light in fabry-perot cavities. *Physics Letters A*, 305:239–244, 2002.
- [14] Peter Fritschel and Rana Adhikari. LHO detector e-log entries. Reference arm length measurement on 21st, July 2002.

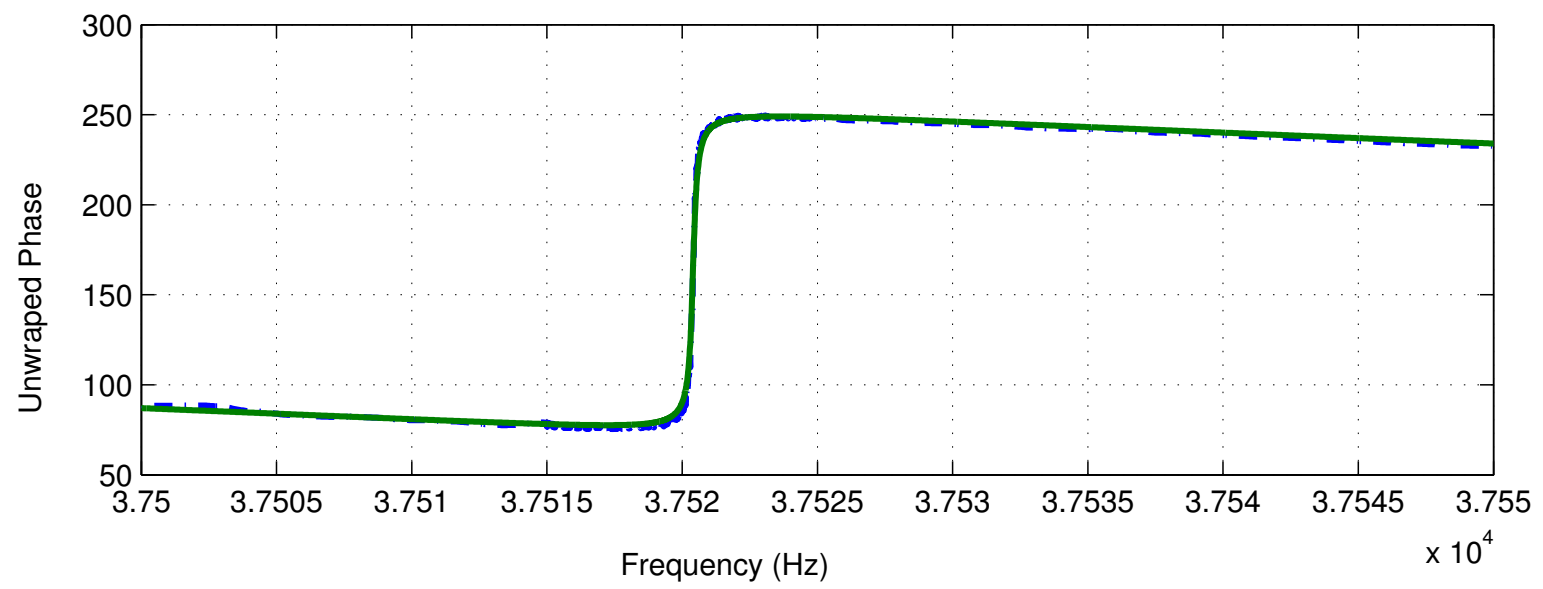
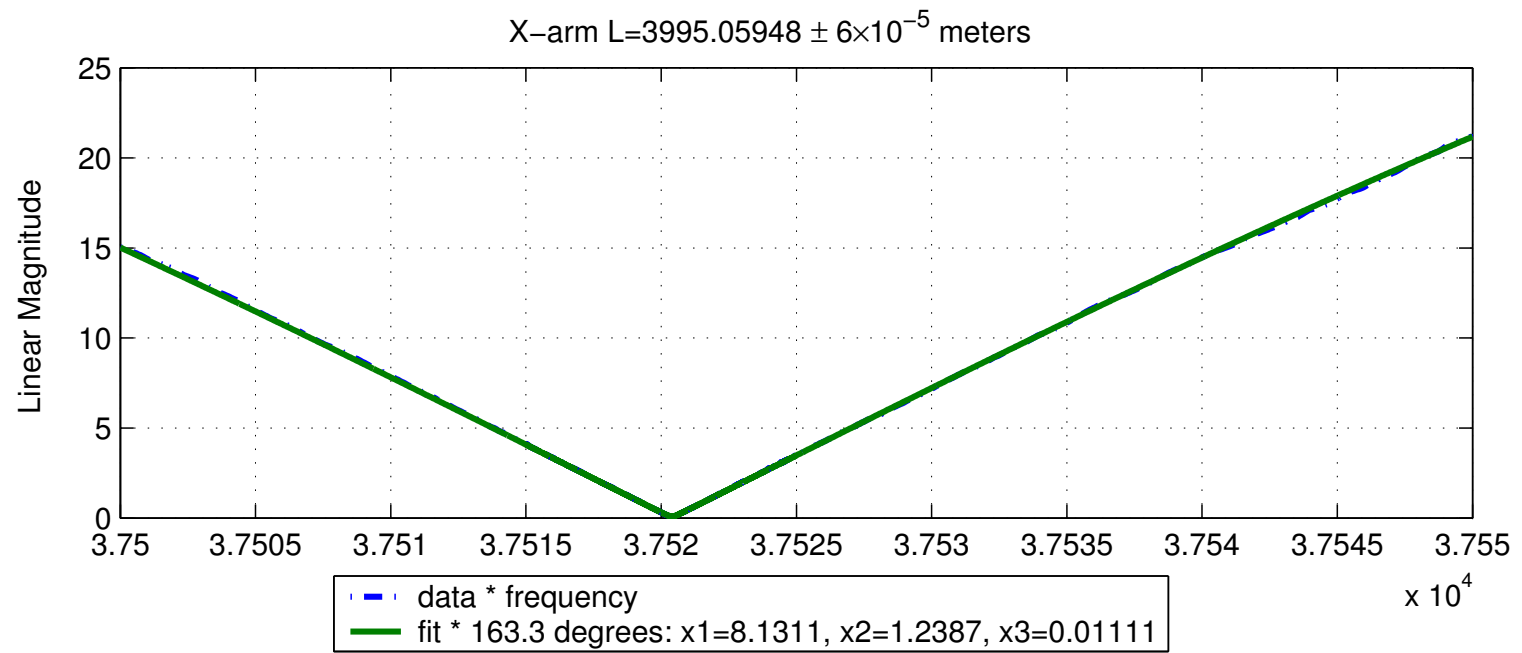


Figure 2: X-arm 1 FSR

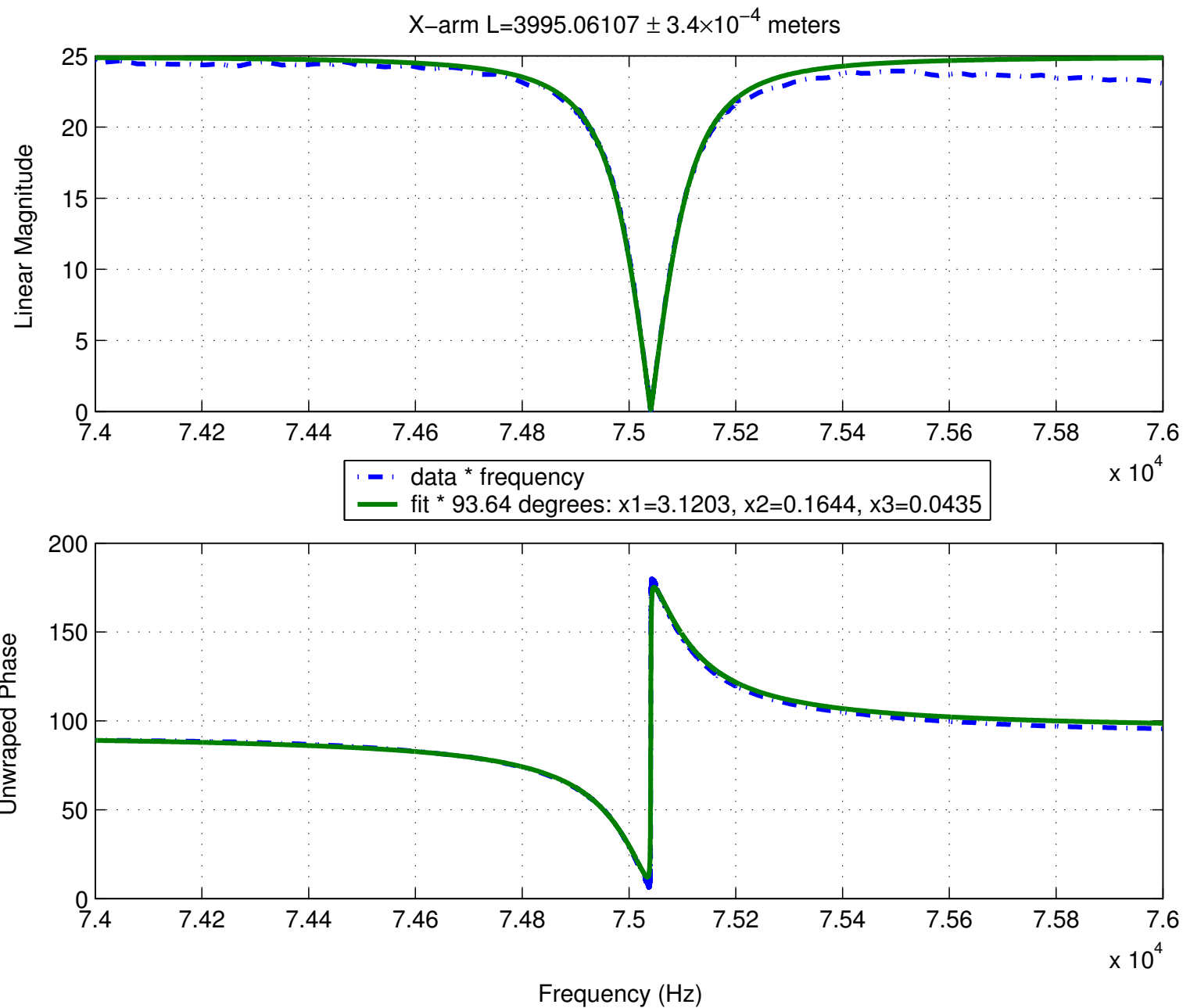
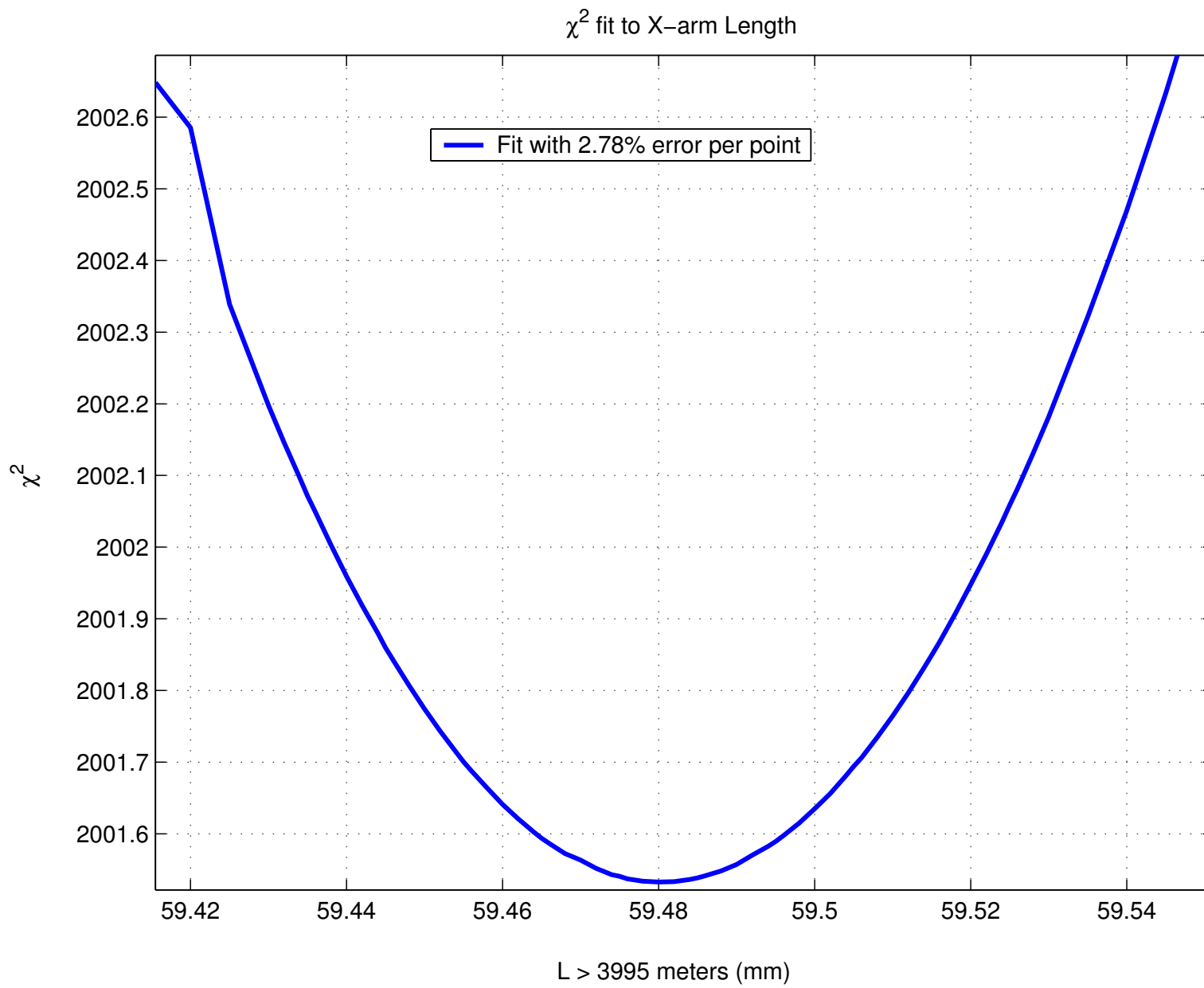


Figure 3: X-arm 2 FSR

Figure 4: Typical chi squared fit for IFO arm length



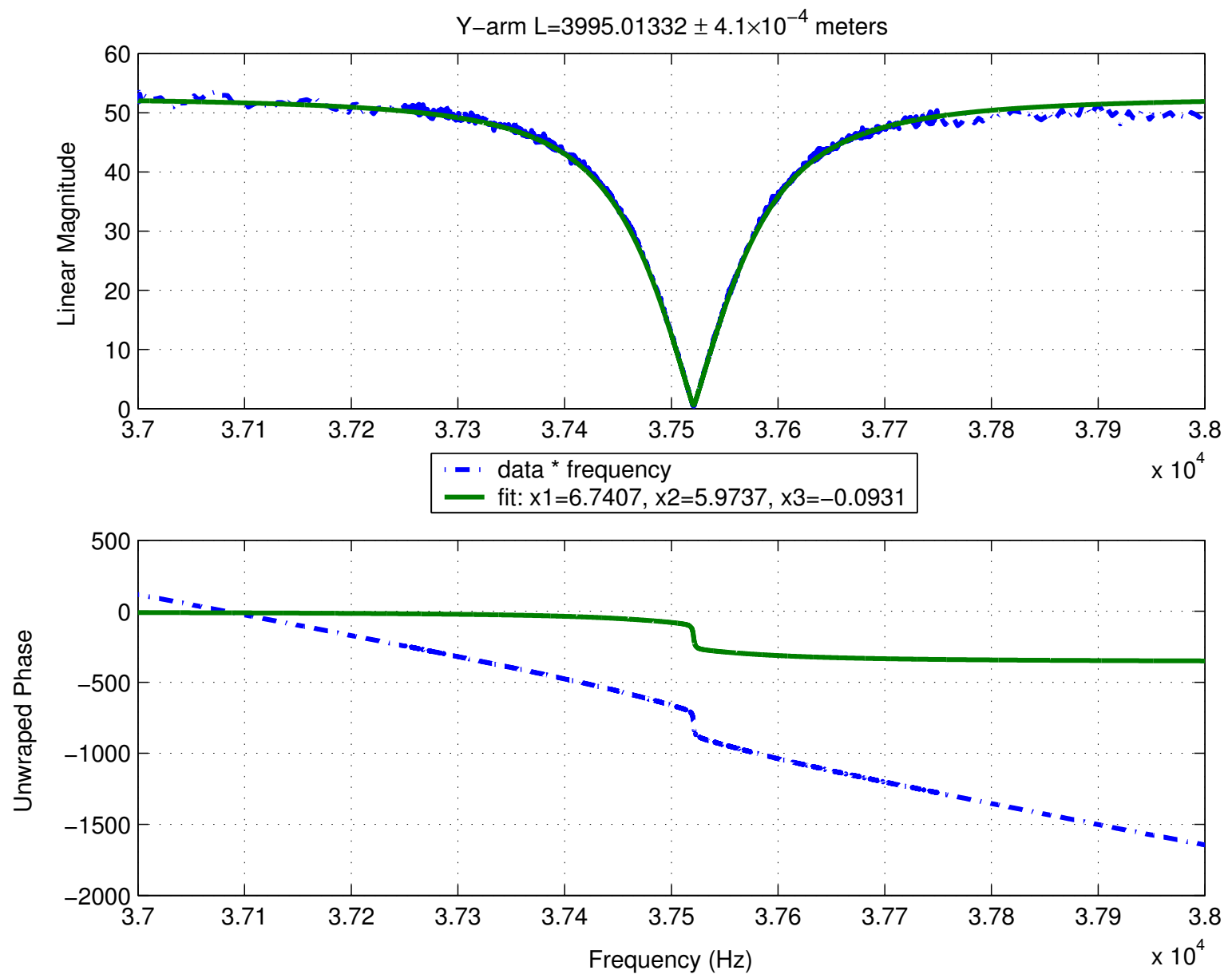


Figure 5: Y-arm FSR, I-phase

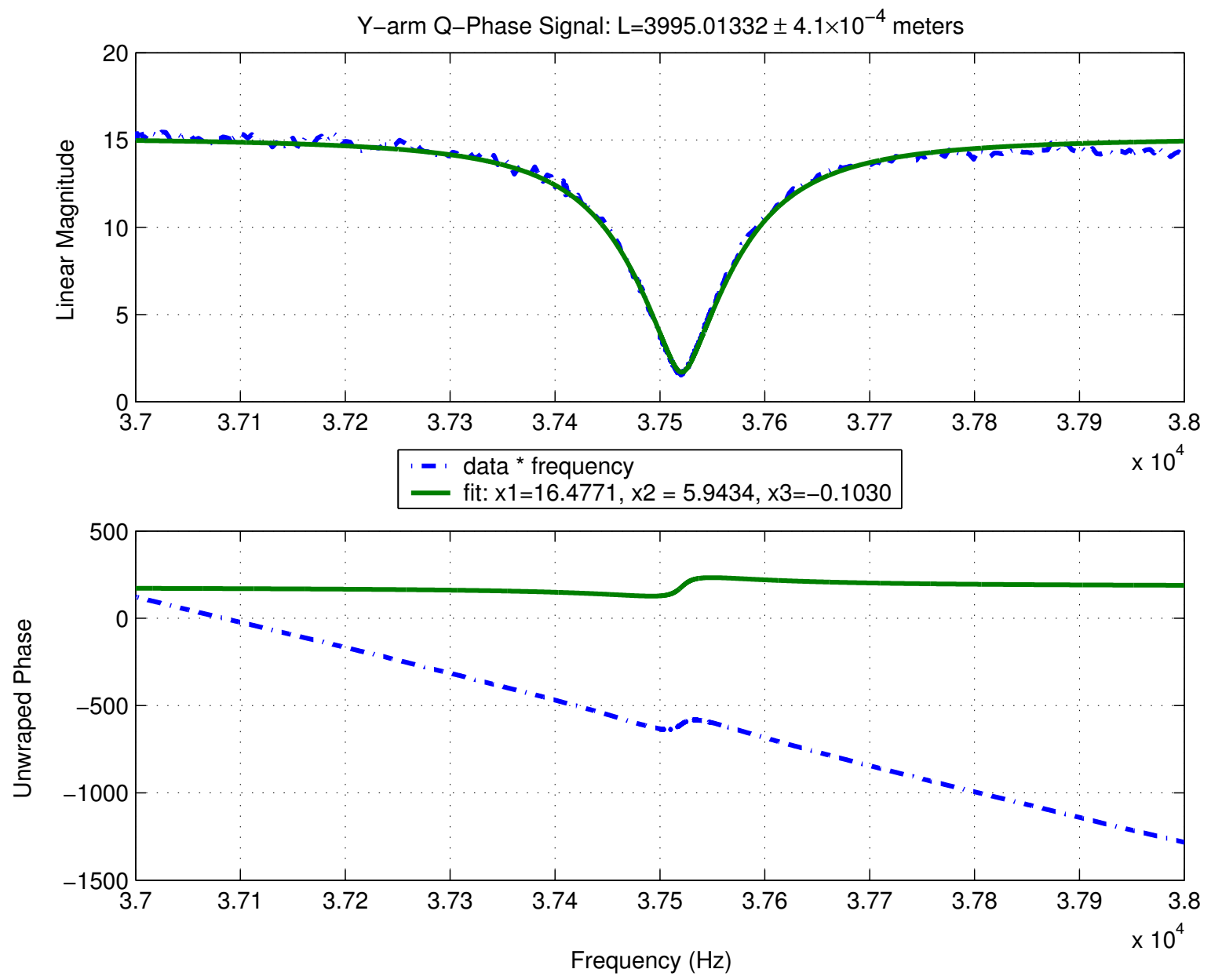


Figure 6: Y-arm FSR, Q-phase

Y-arm:  $L=3995.01332 \pm 4.1 \times 10^{-4}$  meters

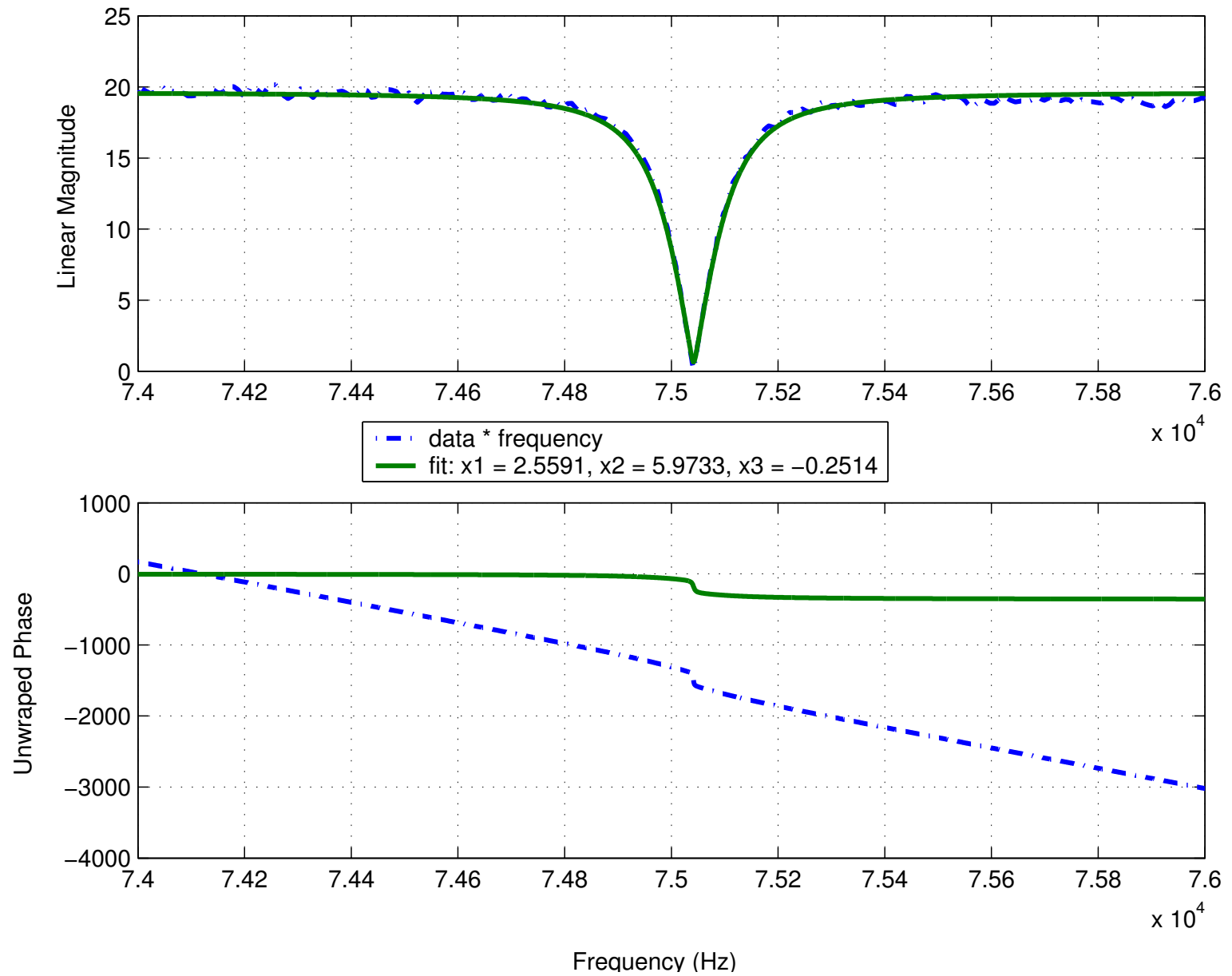


Figure 7: Y-arm 2 FSR, I-phase



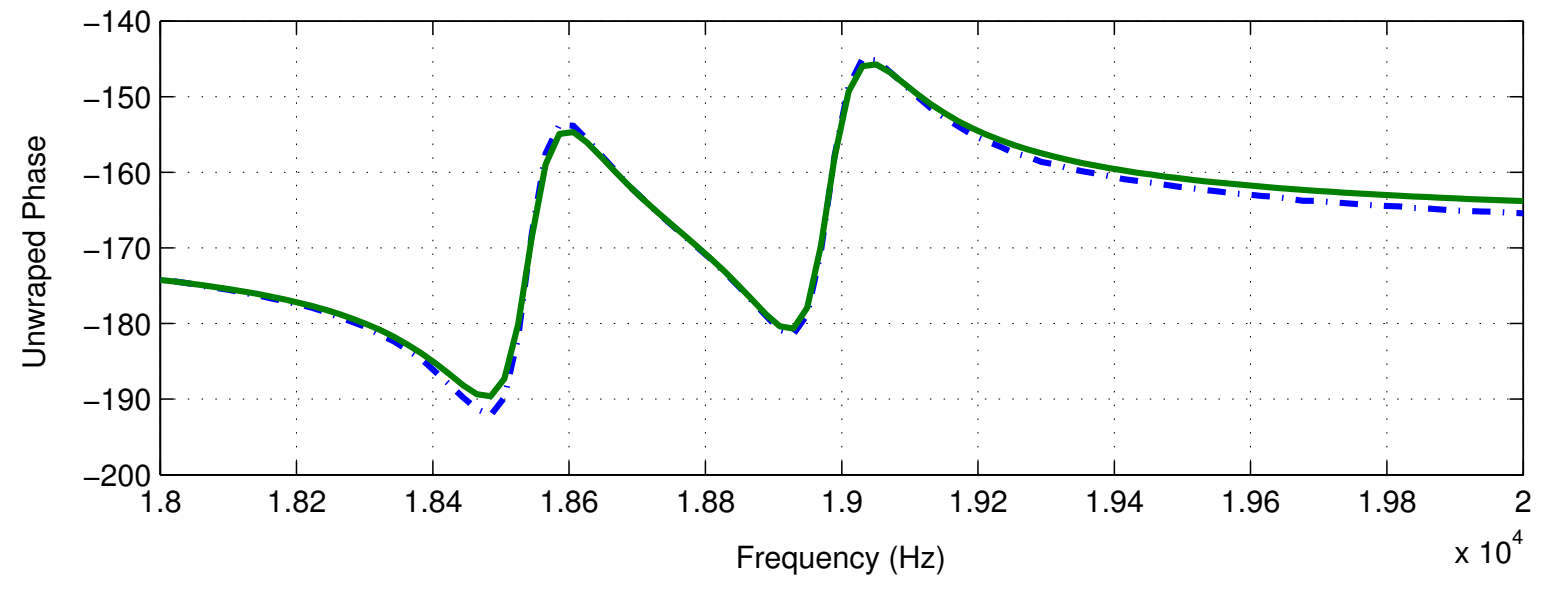
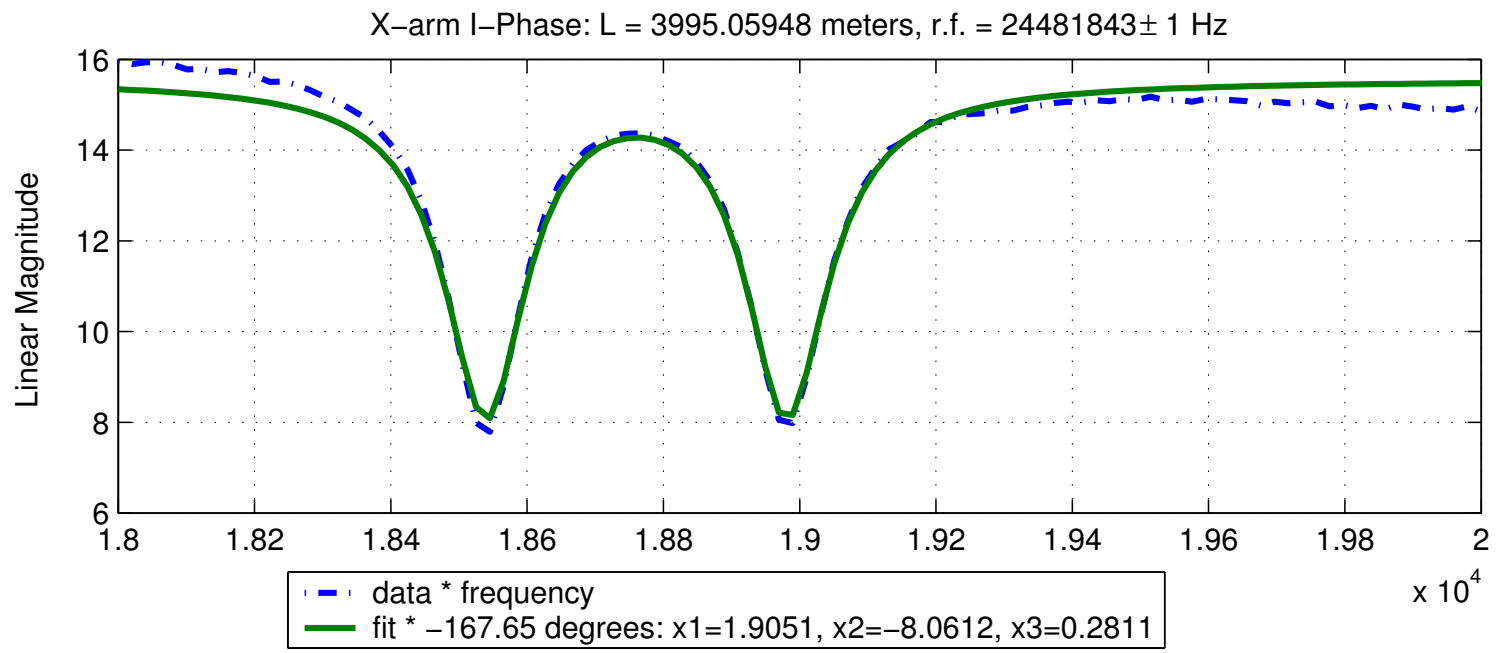


Figure 8:  $\frac{1}{2}$ FSR, I-phase

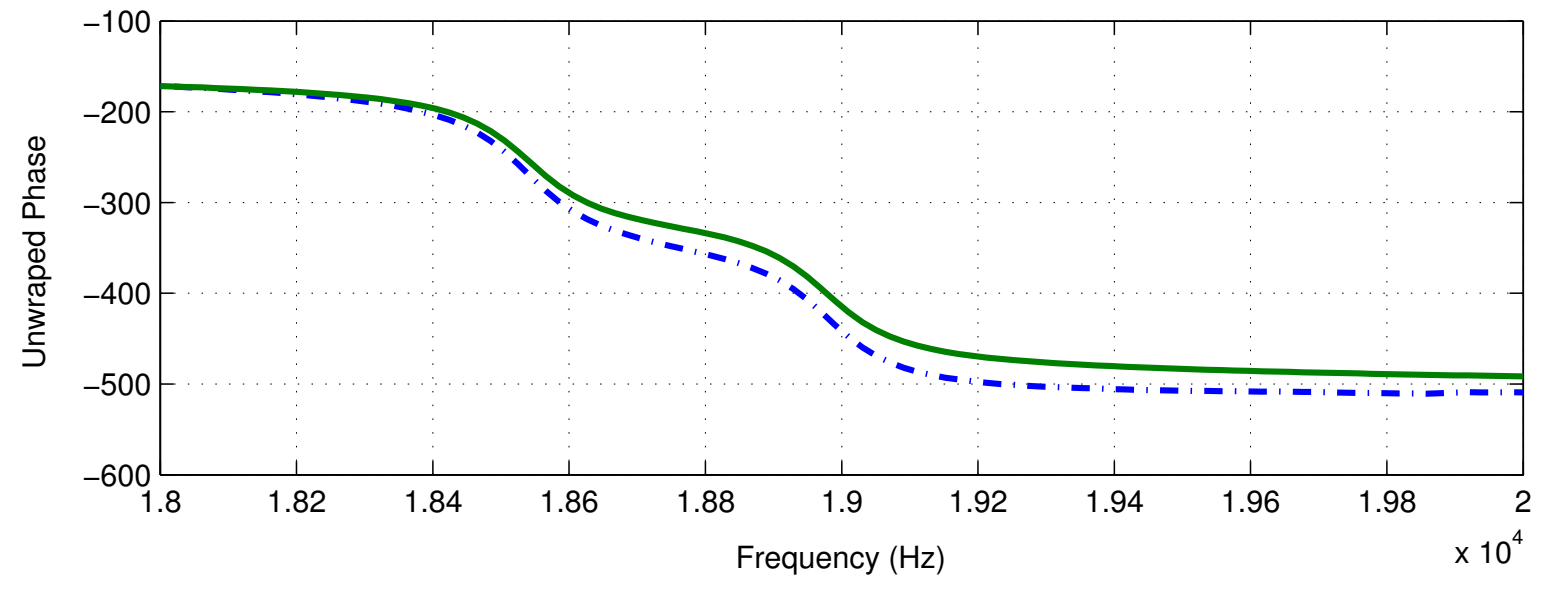
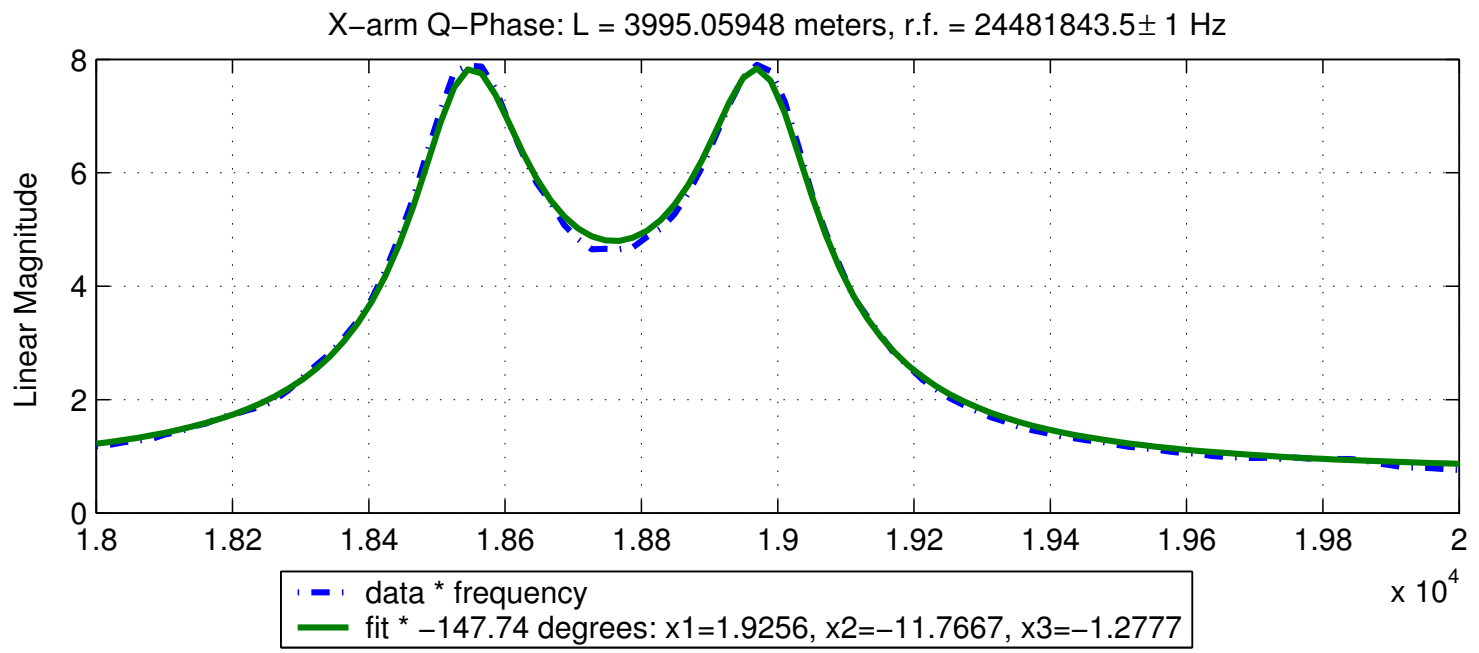


Figure 9:  $\frac{1}{2}$ FSR, Q-phase

X-arm I-Phase: L = 3995.05948 meters, r.f. = 24481843.5 ± 1 Hz

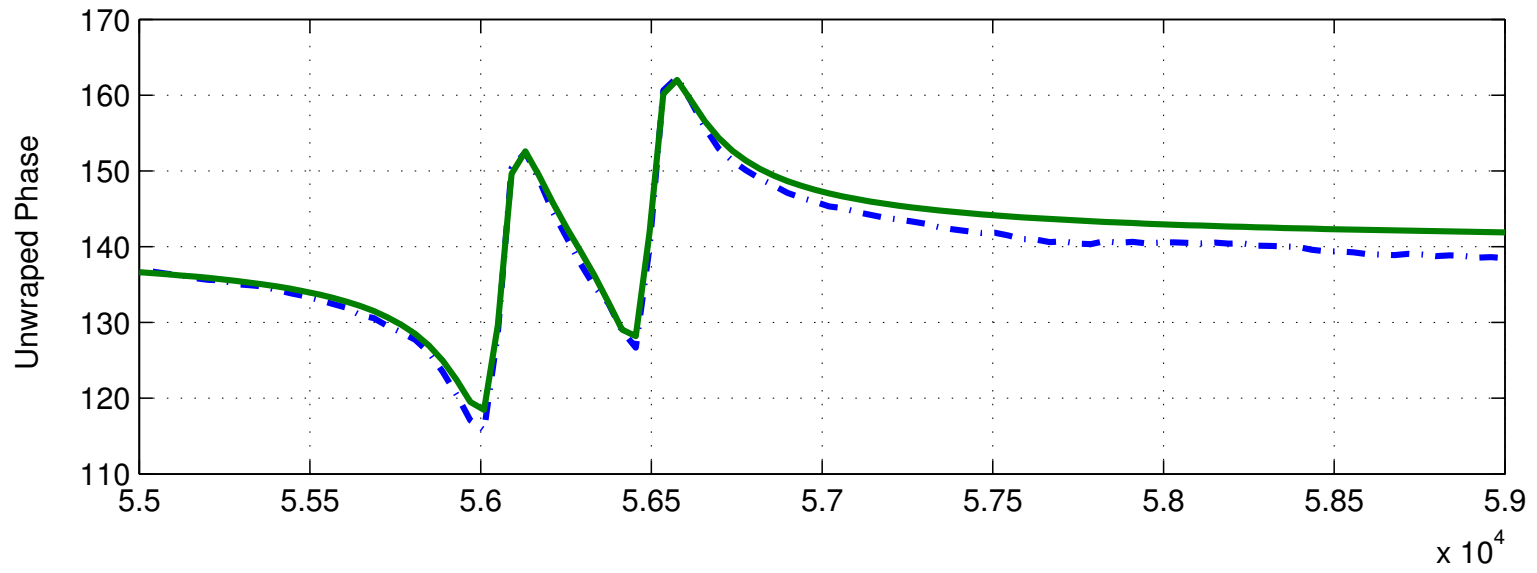
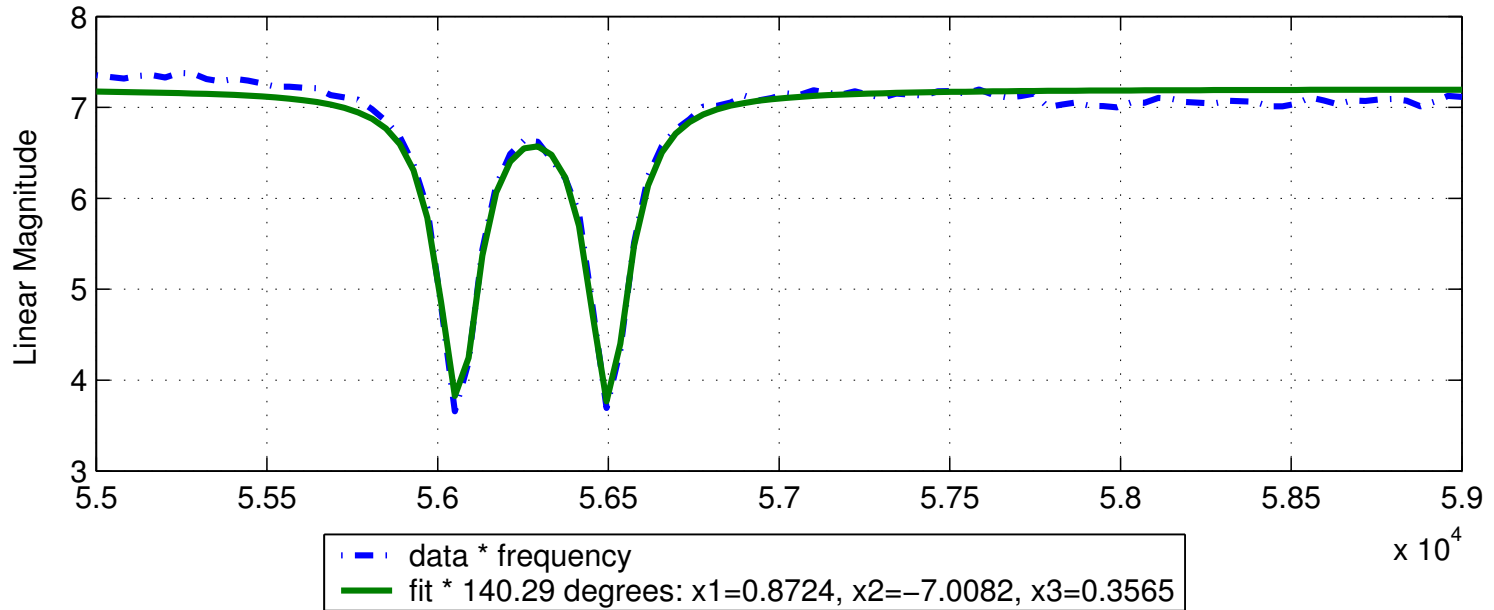


Figure 10:  $\frac{3}{2}$ FSR, I-phase

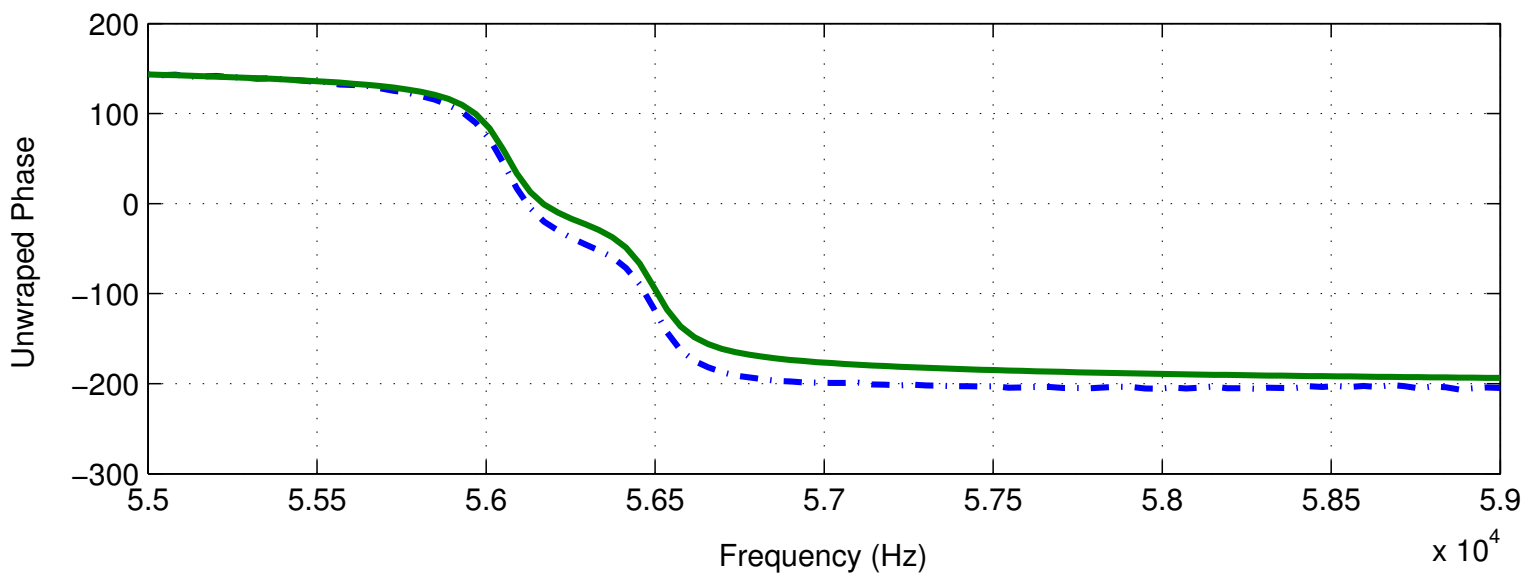
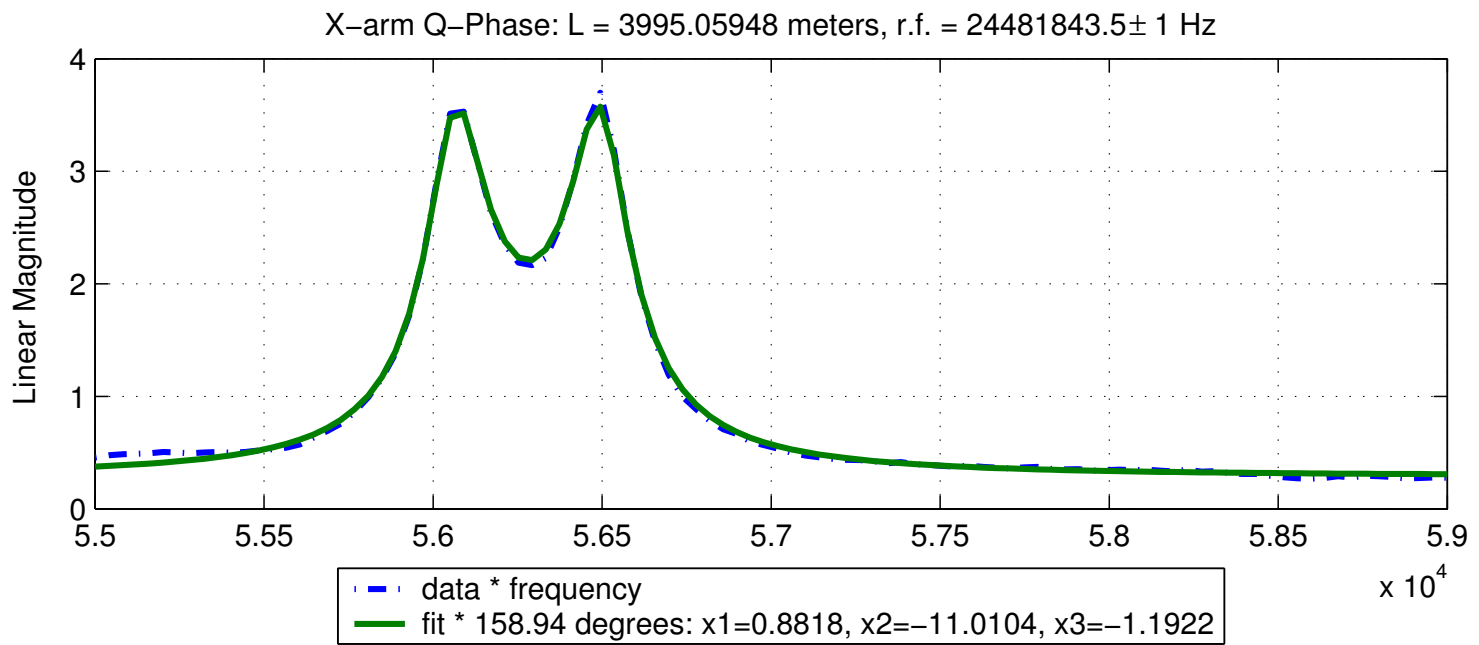


Figure 11:  $\frac{3}{2}$ FSR, Q-phase

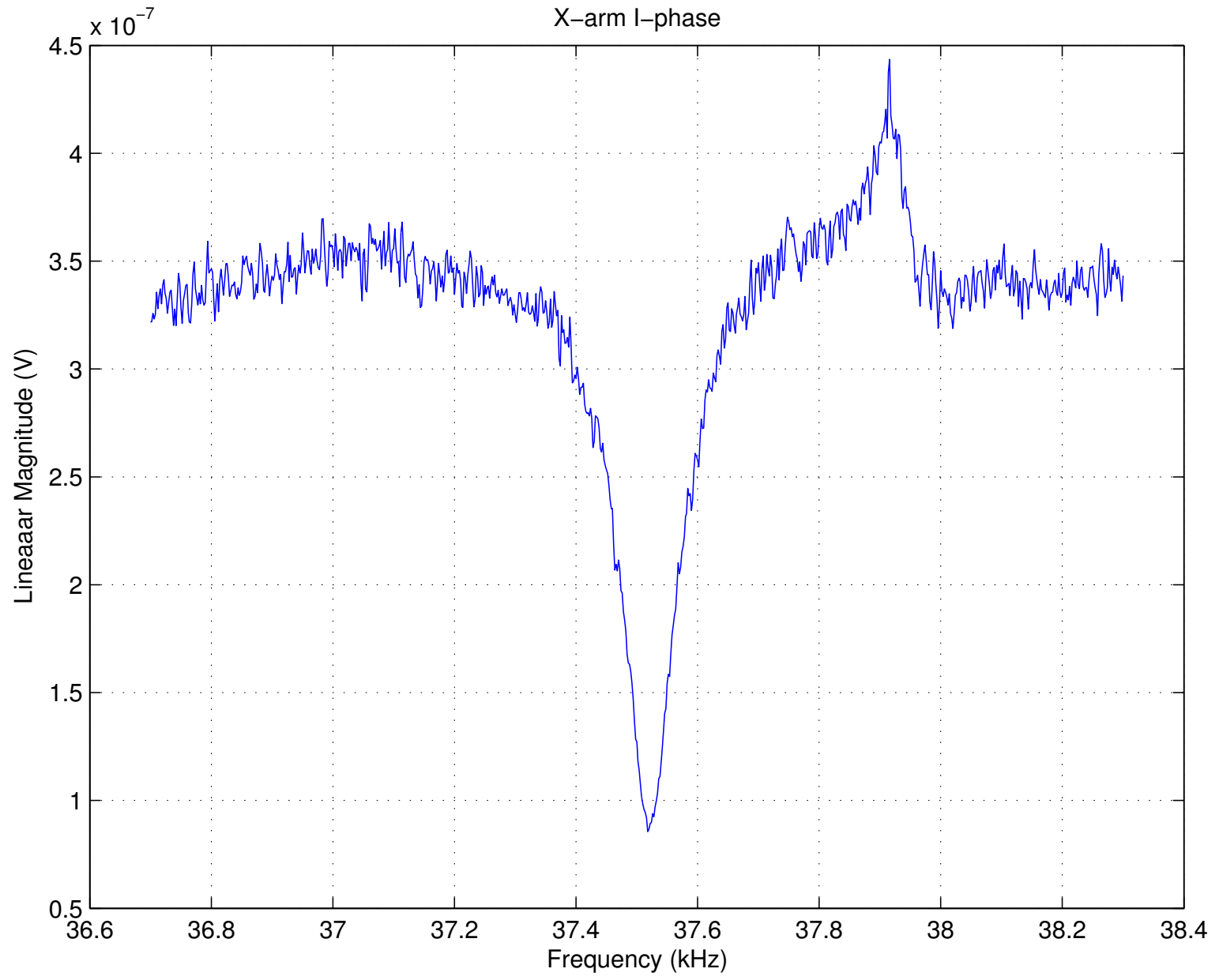


Figure 12: FFT of X-arm signal with no excitation